ACS APPLIED MATERIALS & INTERFACES

Research Article

Cite This: ACS Appl. Mater. Interfaces 2018, 10, 5404−5412

www.acsami.org

Scalable High-Performance Ultraminiature Graphene Micro-Supercapacitors by a Hybrid Technique Combining Direct Writing and Controllable Microdroplet Transfer

Daozhi Shen,[†] Guisheng Zou,[†] Lei Liu,[*,†] Wenzheng Zhao,[†] Aiping Wu,[†] Walter W. Duley,[‡] and Y. Norman Zhou[§]

[†]Department of Mechanical Engineering, State Key Laboratory of Tribology, Tsinghua University, Beijing 100084, P. R. China

[‡]Department of Physics and Astronomy and [§]Department of Mechanical & Mechatronics Engineering, University of Waterloo, Waterloo, Ontario N2L 3G1, Canada

Supporting Information

ABSTRACT: Miniaturization of energy storage devices can significantly decrease the overall size of electronic systems. However, this miniaturization is limited by the reduction of electrode dimensions and the reproducible transfer of small electrolyte drops. This paper reports first a simple scalable direct writing method for the production of ultraminiature microsupercapacitor (MSC) electrodes, based on femtosecond laser reduced graphene oxide (fsrGO) interlaced pads. These pads, separated by 2 μm spacing, are 100 μm long and 8 μm wide. A second stage involves the accurate transfer of an electrolyte microdroplet on top of each individual electrode, which can avoid any interference of the electrolyte with other electronic components. Abundant in-plane mesopores in fsrGO induced by a fs laser together with ultrashort interelectrode spacing enables MSCs to exhibit a high specific capacitance (6.3 mF cm^{-2} and 105 F cm^{-3}) and ~100% retention after 1000 cycles. An all graphene resistor−capacitor (RC) filter is also constructed by combining the MSC and a fsrGO resistor, which is confirmed to exhibit highly enhanced performance characteristics. This new hybrid technique combining fs laser direct writing and precise microdroplet transfer easily enables scalable production of ultraminiature MSCs, which is believed to be significant for practical application of micro-supercapacitor microelectronic systems.

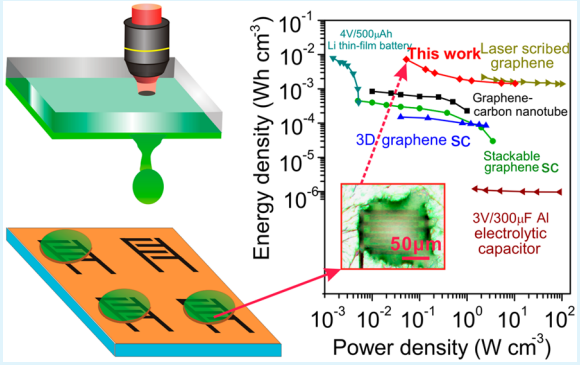

KEYWORDS: *graphene, micro-supercapacitors, laser direct writing, mesopores, microdroplet*

INTRODUCTION

The continued demand for the miniaturization of electronic devices used as implantable biosensors,[1−4] microrobots,[5−7] micro-electromechanical systems (MEMS),[8−10] and portable and wearable personal electronics[11,12] is driven by the need for enhanced functionality, speed of operation, and reliability. It has been found, however, that most of the weight and volume in such devices arise from the incorporation of conventional integrated energy storage units. These components limit the miniaturization of the overall system,[13] resulting in an increased demand for rechargeable energy storage devices with enhanced performance that are small enough to be encapsulated in micro/nano electronic devices. The miniaturization of power sources remains challenging because the performance of energy storage components does not scale well with a reduction in size. These components are also not compatible with on-chip integrated processing.[13−16]

Among these energy storage devices, micro-supercapacitors (MSCs) have now emerged as a family of micro energy storage devices combining high power density, fast charge/discharge rates, long service life, and fully planar platform geometry.[17−19] This device structure is superior because of the ability to control and shorten electron/ion diffusion paths[19,20] and the ease of on-chip encapsulation together with other micro-electronic systems, which is vital for miniature microdevices and nanodevices.[15,16] To date, most refinements in the performance of MSCs have focused on electrode material engineering to increase energy density and charge/discharge rate combined with flexibility.[21−26] Few studies have focused on the compact encapsulation and miniaturization of MSCs <100 μm[27,28] as it is hindered by[28] (1) decreasing electrode dimensions while maintaining overall performance and (2) accurate transfer of liquid/gel electrolyte drops to interlaced electrode patterns without interference with other electronic components in microsystems. In this context, Meng et al.[27] have reported 720 μm all-solid-state MSCs with 3D micro-integration capability, and Lobo et al.[28] have reported the formation of electrodes (40 μm long and 1 μm interelectrode

Received: September 22, 2017
Accepted: January 22, 2018
Published: January 22, 2018

DOI: 10.1021/acsami.7b14410
ACS Appl. Mater. Interfaces 2018, 10, 5404−5412

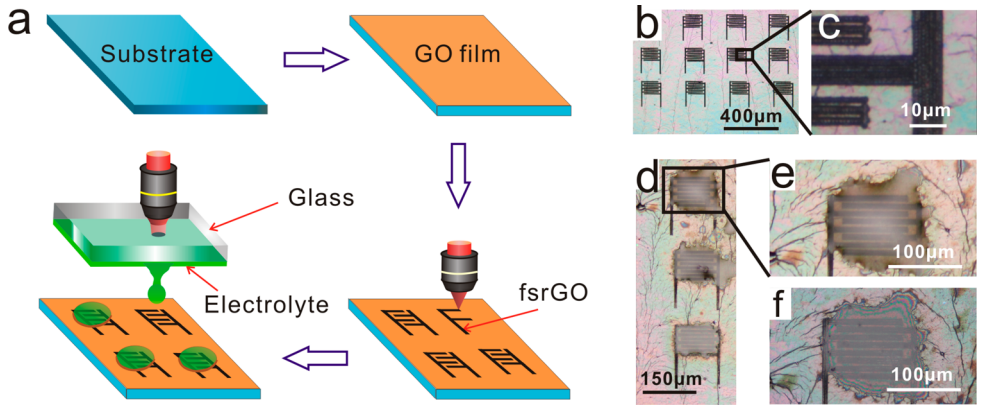

Figure 1. Fabrication process for integrated MSCs on a GO film using fs laser processing. (a) Si wafer with a SiO_2 layer is coated with a GO film followed by direct writing with fs laser radiation to produce interlaced rGO microelectrodes. The microelectrolyte droplet is transferred on top of the interlaced microelectrodes using the fsLIFT technique. (b, c) Interlaced rGO electrode arrays maintain high resolution with a spacing of ∼2 μm between individual fingers. (d) Microelectrolyte droplets exactly cover the electrode array. (e) MSC after transfer of the electrolyte and (f) after being left overnight at room temperature to remove extra water.

spacing) in graphene oxide (GO) using a focused ion beam (FIB) together with drop-casting of an electrolyte gel. Although FIB reduced GO (FIB-rGO) electrodes was ultraminiature, the electrolyte drops assumed to precisely cover the electrodes were too small (40 μm with a volume of ∼30 pL) to be drop-cast without contaminating other functional electronic components. A feasible transfer technique needs to be developed to deposit electrolyte drops precisely on micro-electrodes to produce ultraminiature MSCs for incorporation and encapsulation in ultracompact micro/nanoelectronic systems.

Femtosecond laser-induced forward transfer (fsLIFT) is a well-studied methodology for deposition of various materials such as inks,[29] metals,[30] and silicon[31] with very high resolution. fsLIFT is a single-step direct printing technique that can be used for the deposition of nanoscale and microscale components. A high-power fs laser beam, tightly focused on the target, results in a narrow jet of liquid.[30,31] This is an ideal method for the transfer of electrolyte microdroplets for engineering of MSCs.

In this paper, we report a simple scalable direct writing method for the production of ultraminiature micro-supercapacitor (MSC) electrodes, based on fs laser reduced graphene oxide (fsrGO) interlaced pads separated by 2 μm spacing. Following this procedure, a microdroplet electrolyte gel is then accurately transferred on single individual fsrGO electrodes using the fsLIFT technique. The precise cover avoids any interference of the electrolyte with other electronic components. The results show that the abundant in-plane mesopores in reduced GO (rGO) induced by the fs laser together with the ultrashort interelectrode spacing leads to a large electrochemical capacitance and enhanced power/energy density. An all-graphene micro resistor−capacitor (RC) filter constructed by combining a fsrGO resistor and an as-prepared MSC having precise cover of electrolyte is found to exhibit much higher filter efficiency than that seen in another RC filter that has a MSC covered by a large uncontrollable electrolyte drop which easily contaminates the fsrGO resistor nearby. The enhanced performance characteristics of this all graphene microdevice approve the priority and irreplaceability of fsLIFT for application of ultraminiature micro-supercapacitor in micro-devices. This new hybrid technique combining fs laser direct writing technology and accurate microdroplet transfer is believed to innovatively provide a practical route to decrease the overall size of microelectronic systems.

RESULTS AND DISCUSSION

Figure 1a illustrates the fabrication process of MSCs on a silicon oxide wafer. A thin GO film is first coated on silicon oxide by drop-casting a GO dispersion. This is then annealed at 80 °C for 30 min in air. The as-prepared GO film is then irradiated by fs laser pulses focused by a microscope objective with ×100 magnification. The GO is reduced as oxygen atoms are eliminated in a photochemical process driven by fs laser radiation. This processing produces rGO with enhanced conductivity (see Table S1). The ultratightly focused laser shows high resolution (Figure S5) enough to write ultra-miniature electrodes with ∼2 μm interelectrode spacing (see Figure 1b,c), which is comparable in size to those obtained in FIB-rGO patterns.[28] Compared to FIB processing, fs laser direct writing is more cost-effective and practical since it is carried out in air at atmospheric pressure. Following irradiation, the glass was coated with poly(vinyl alcohol)−sulfuric acid ($PVA-H_2SO_4$) gel as a donor substrate for transfer of electrolyte droplets of ∼50 μm in diameter. Afterward, single fs laser pulses were focused with a microscope objective with ×10 magnification through the glass onto the electrolyte gel donor film. Explosive expansion of the electrolyte gel[29,30,32,33] then results in the ejection of a microdroplet from the donor film. The high-velocity trajectory precisely deposits the particle on the surface of the patterned microelectrodes just below the donor substrate. The small electrolyte droplet can exactly cover the single microelectrode target without contacting other electrodes nearby (see Figure 1d). The size of the electrolyte droplet can be controlled by adjusting the laser pulse energy (see Figure S6) and can be as small as 20 μm under optimized conditions.[29,34] The electrolyte gel droplet eventually solidifies and shrinks in height after the evaporation of water (Figure 1e,f). The droplet transferred under explosive pressure may be also irradiated by the fs laser; however, this process does not affect the value of potential of hydrogen (pH) and seems not reducing the performance of $PVA-H_2SO_4$ gel as electrolyte in supercapacitors (Figure S12).

The fs laser reduction of GO is caused by a strong photochemical effect that results in deoxygenation of GO.[16,18,35,36] The reduction process is initiated by the

DOI: 10.1021/acsami.7b14410
ACS Appl. Mater. Interfaces 2018, 10, 5404−5412

photoexcitation of C═O bonds, which results in the preferential removal of oxygen since the binding energy of C═O is much smaller than that of sp^2 C−C bonds.[28,37] X-ray photoelectron spectroscopy and Raman spectroscopy were used to investigate the deoxygenation process. Figure 2a

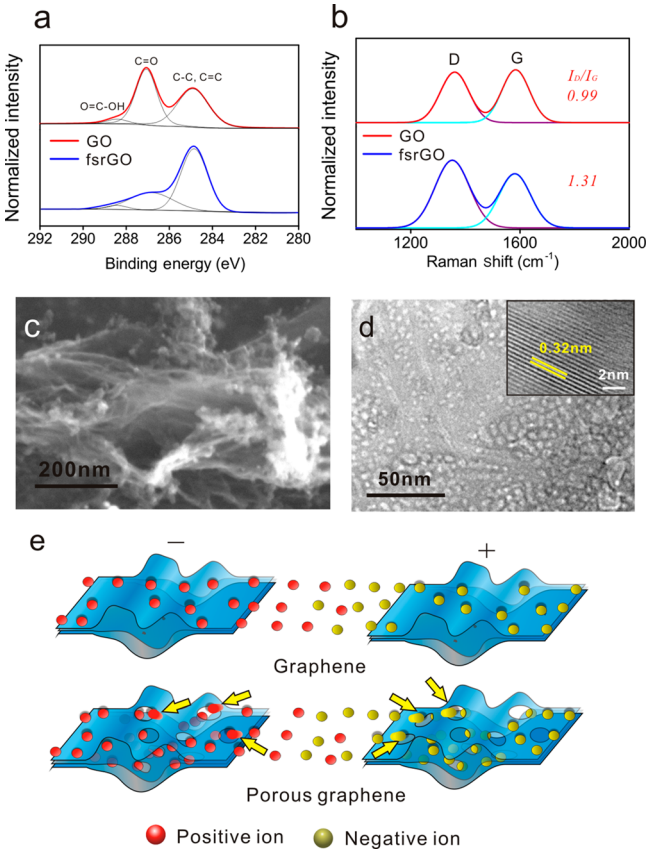

Figure 2. Characterization of fsrGO. (a) XPS spectra and (b) Raman spectra of GO and fsrGO (c) SEM and (d) high-resolution images of fsrGO. Abundant mesopores (diameter ∼10 nm) exist in fsrGO. (e) Schematic showing ionic pathways involved in charge transport in graphene and in porous graphene electrodes during charging of the supercapacitor. In the absence of stacking, ions are primarily transported and stored on the surface of nonporous graphene sheets. When mesopores are present, ions can migrate through the mesopores and are then stored on subsurface graphene sheets. This process improves the specific surface area and ion diffusion dynamics.

compares high-resolution C 1s spectra of GO and fsrGO. The two main contributions to the overall peak of GO are the C−C peak at 284.8 eV and the peak at 287.1 eV associated with C═O groups. The C 1s spectrum shows that the content of carbon not bounded to oxygen in GO is estimated to be ∼45.7%, while the fsrGO shows much higher content (70.7%). Thus, the reduction of GO is relatively successful and fsrGO shows a notably enhancement of conductivity comparing to GO (see Table S1). The decrease in the strength of the C−O peak in fsrGO relative to that in GO is ascribed to the deoxygenation process during fs laser irradiation. Raman spectra of the GO film display two broad peaks corresponding to the D and G band peaks (Figure 2b). These peaks have identical profiles and widths after laser reduction, indicating that laser irradiation introduces no amorphization of the GO film.[28,38,39] This is also apparent from the clear spacing lines (the inset in Figure 2d) and hexagon diffraction pattern of fsrGO (Figure S7). Laser reduction of GO does, however, increase the I_D/I_G ratio from 0.99 to 1.31, which shows that fs laser irradiation results in structural changes and an increased defects concentration.[18,40,41] Figure 2c and d show that the fsrGO sheets have many mesopores each having a diameter of <10 nm (Figures S8−S10). Defects associated with the edges of these mesopores are likely responsible for the observed increase in the I_D/I_G ratio in Raman spectra (Figure 2b).

The mesopores seen in the graphene film after fs laser irradiation on GO can be attributed to two primary and related mechanisms: (1) localized etching by hydrogen peroxide generated from laser-induced water breakdown and (2) laser-induced decomposition similar to that occurring in coal gasification processes.[42] The as-prepared GO film contains high water content due to selective superpermeability of a GO membrane to water molecules when placed in air.[43−45] When the fs laser irradiates GO, the peak power density at the laser focus reaches up to ∼10^{14} W cm^{-2}, which strongly leads to the photoionization and photodissociation of water molecules producing H, O, and OH radicals and radical ions. These species then react together and form H_2O_2 molecules which act to etch the GO sheets and result in mesopores.[46] Process 2 is similar to that occurring in the gasification of coal. Gasification occurs when solid carbon-based materials react with oxygen, water, and carbon dioxide to produce fuel-rich products.[42] Russo et al.[42] suggested this is initiated at sp^3 carbon sites and is the main process responsible for the formation of mesopores in GO during fs laser ablation of graphite in water.

Although, in theory, graphene has a remarkable specific surface area for ion storage, graphene sheets are prone to restack via $\pi-\pi$ interaction and van der Waals bonding to form layered agglomerates. Restacking inhibits ion transport into internal graphene layers as shown in Figure 2e, causing a significant reduction in specific surface area and a much lower mass diffusion rate.[19,40,47] By introducing mesopores in the graphene sheets, ions can diffuse through the mesopores to the inner graphene layers in stacks of graphene sheets as shown in Figure 2e. As a result, mesopores induced by fs laser irradiation will increase the effective surface area and lead to enhancement in the dynamics of ion diffusion.

The effect of the mesopores introduced in GO by fs laser irradiation is also expected to be similar to that of high-resolution planar fins introduced into miniaturized fsrGO electrodes. Such features of planar fins and mesoporous structures enhance the electrode/electrolyte contact area and improve electron/ion diffusion paths when used as electrode materials in energy storage devices.[19,28,40,41,47] In the present study, the electrochemical performance of miniaturized fsrGO MSCs was evaluated by cyclic voltammetry (CV), galvanostatic charge/discharge (GCD), and electrochemical impedance spectroscopy (EIS).

CV curves of fsrGO MSCs are found to be semisigmoidal and reversible (Figure 3a and Figure S13). This indicates the emergence of radial diffusion as the dimensions decrease due to the miniaturization of the interlaced pads in electrodes.[48,49] A similar effect is seen in ultrasmall FIB-rGO MSCs.[28] As the size of the electrode decreases, the contribution of convergent diffusion to the voltammetry increases so that faster mass transport per unit area of the electrode was obtained, causing larger current densities and voltammograms[48,49] (Figure S16) which yields the observed shape of the CV curves with enhanced current density. As estimated, the CV curves of MSCs with larger fsrGO finger electrodes width with separated

DOI: 10.1021/acsami.7b14410
ACS Appl. Mater. Interfaces 2018, 10, 5404−5412

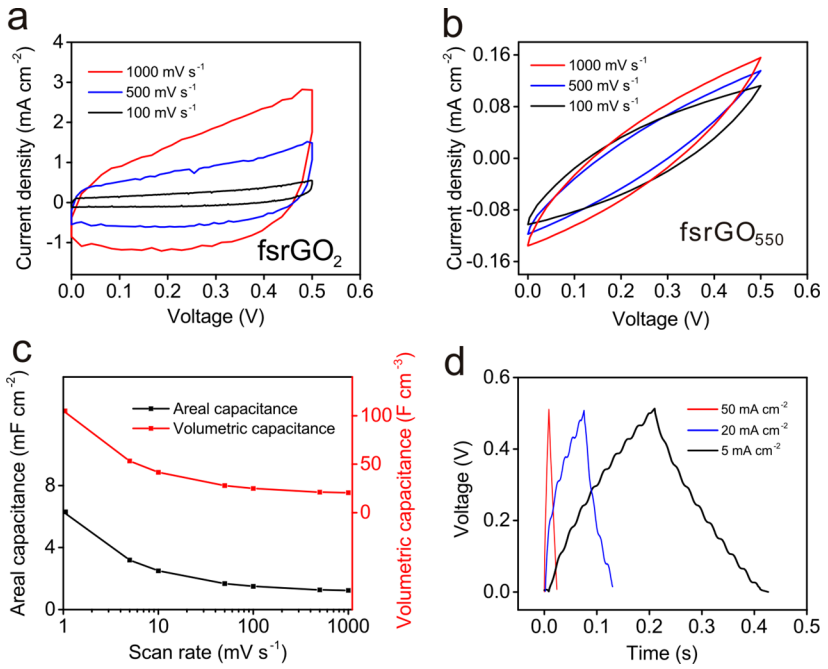

Figure 3. Electrochemical performance of the fsrGO-MSC in a PVA-H_2SO_4 electrolyte. CV profiles of fsrGO MSC with interelectrode spacing of (a) 2 μm and (b) 550 μm obtained at a scan rate of 100, 500, and 1000 mV s^{-1}. (c) Specific capacitance versus scan rate in ultraminiature fsrGO MSCs. (d) Galvanostatic charge/discharge plots of fsrGO$_2$ MSC at a current density of 5, 20, and 50 mA cm^{-2}.

distance of 550 μm (fsrGO$_{550}$) show a very low current densities as illustrated in Figure 3b. The specific capacitance of fsrGO$_{550}$ is only 0.037 mF cm^{-2} at the scan rate of 1000 mV s^{-1}, which is 33 times less than that of fsrGO MSC with interelectrodes spacing of 2 μm (fsrGO$_2$). This indicates that the miniaturization of MSC electrodes indeed increases the specific capacitance density. It seems that this miniaturization, however, reduces the potential window of MSCs (compare Figure 3a with Figure S11). This narrow potential window might be attributed to the easier migration of oxygen atoms in GO under the same electric field because of the ultrashort distance of interelectrodes spacing,[50] which was also seen in the reported ultraminiature graphene MSC reduced by FIB.[28]

Figure 3c shows the ultraminiature fsrGO MSCs have a relatively high specific capacitance. The areal capacitance at scan rate of 1 mV s^{-1} is ~6.3 mF cm^{-2}. The atom force microscopy (AFM) image (see Figure S3) shows that the thickness of fsrGO is only ~0.6 μm; hence, the volumetric capacitance is as high as ~105 F cm^{-3}. At this scan rate, the gravimetric capacitance is estimated to be 86.7 F g^{-1}. The areal capacitance at a scan rate of 10 mV s^{-1} is 2.5 mF cm^{-2}, ~200 times higher than that found in MSCs prepared from plasma-reduced GO (0.1 mF cm^{-2})[17] and 2 times higher than that in laser-written porous carbon MSCs.[51] The volumetric capacitance at a scan rate of 10 mV s^{-1} is 41 F cm^{-3}, which is ~10 times higher than that reported in laser scribed graphene MSC (3.05 F cm^{-3})[16] and 20 times higher than in MSCs produced using plasma-reduced GO (2 F cm^{-3}).[17] The so high volumetric capacitance of fsrGO MSCs is attributed to the relatively high area capacitance as well as the ultrathin electrodes. Even though, the specific capacitance of fsrGO MSC is still less than that of FIB-rGO MSCs (102 mF cm^{-2} and 1700 F cm^{-3} at scan rate of 1 mV s^{-1}) because of the incompletely reduction of GO by the fs laser compared with reported FIB-rGO.[28] This also implies that the specific capacitances can be further improved by increasing the conductivity of fsrGO electrodes through optimized laser directing parameters in future studies.

From the above comparison, it can be seen that specific capacitances of fsrGO MSCs show major improvement compared to that of most other graphene supercapacitors reported. The edge effect, arising from the enhanced mass flux during electrochemical test when electrodes size reduces, plays an essential role in the remarkable improvement of specific capacitances. This effect becomes even more important when the electrode size is ~10 μm.[48] In our case, each fsrGO electrode has an ultraminiature size with width of only 10 μm, which leads specific capacitance exhibiting 33 times higher than that of MSCs with fsrGO electrode width of 550 μm (Figure 3a,b). This remarkable difference indicates that the ultraminiature size of fsrGO electrodes indeed increases the calculated capacitances due to the edge effect. To our best knowledge, however, the width of almost all reported graphene electrodes is >150 μm, meaning >15 times larger than that of our fsrGO MSCs. Thus, it is not surprising that the calculated specific capacitances of fsrGO ultraminiature MSCs are enhanced. In addition, the unique mesoporous network structure of fsrGO electrodes also helps to minimize the pathway for ion diffusion from the electrolyte to the electrode material and increases the specific surface area of graphene sheets that can store ions. The micrometer/submicrometer scale of the interelectrode separation also decreases the diffusion length between adjacent microelectrodes and improves the overall current and energy densities in response to the radial transport of ions at edges of ultrasmall fsrGO pads. Thus, the edge effect due to the reduced size of fsrGO electrodes, together with existence of abundant mesopores and ultrathin fsrGO film, results in the major improvement of calculated specific capacitances of fsrGO MSCs. The specific capacitance shows a very weak dependence on scan rate above 10 mV s^{-1} but is a stronger function of scan rate below 10 mV s^{-1}. However, the fsrGO MSCs retain ~23.8% of their

DOI: 10.1021/acsami.7b14410
ACS Appl. Mater. Interfaces 2018, 10, 5404−5412

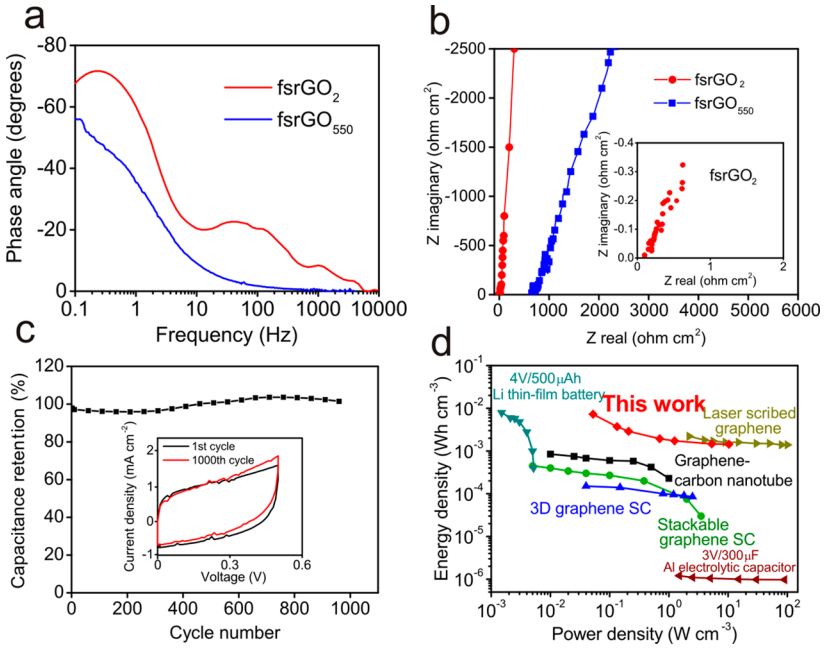

Figure 4. EIS measurements for ultraminiature fsrGO MSCs. (a) Impedance phase angle versus frequency and (b) Nyquist plot of impedance in fsrGO MSCs. (c) Specific capacitance retention in cyclic testing of fsrGO MSCs. Inset shows the initial CV curve (black) and 1000th CV curve (red) at a scan rate of 500 mV s^{-1}. (d) Ragone plot of the current fsrGO MSCs compared with commercial available energy storage systems and recently published data for MSCs.[52−54]

capacitance when the scan rate increases from 1 to 100 mV s^{-1}. This is much higher than in FIB-rGO MSCs which retain only 5% of their capacitance.[28] This implies that fs laser rGO MSCs have an improved rate capability over this charging range.

The galvanostatic charge/discharge (GCD) curves (Figure 3d) of fsrGO MSCs exhibit a nearly symmetrical triangular shape with a small drop in internal resistance (iR) even at the ultrahigh current density of 50 mA cm^{-2}. This confirms that the device has a relatively low equivalent series resistance (ESR). These MSCs have an area specific capacitance of 2.14 mF cm^{-2} (with a volumetric capacitance of 35.7 F cm^{-3}) at 5 mA cm^{-2} and maintain 78% of this value (1.67 mF cm^{-2}) when operated at an ultrahigh current density (50 mA cm^{-2}). The internal surfaces of fsrGO are readily accessible to the electrolyte, and there is very little impediment to ion transport. The device can then maintain high capacitance even when operated at these ultrahigh charge/discharge currents. Despite the large specific capacitance of fsrGO MSCs, the absolute value of peak current measured in CV test is still low (~150 nA for scan rate of 500 mV s^{-1}). This small value of current is easily affected by external fluctuation during CV and GCD test, resulting in unsmooth curves as shown in Figure 3a,d, even though the fluctuation does not affect the reliability of measurement from the cyclic test in Figure 4c, which shows that the deviation of capacitance is less than 5% after 1000 cycles.

Electrochemical impedance spectroscopy (EIS) provides a consistent insight into the power performance (Figure 4). The characteristic frequency f at a phase angle of −45° marks the frequency at which the resistive and capacitive impedances are equal. The corresponding time constant $\tau = 1/f = 476$ ms (Figure 4a) of ultraminiaturized fsrGO MSCs is lower than seen in active carbon-based MSCs ($\tau = 700$ ms) or onionlike carbon-based macrodevices ($\tau > 1$ s). Also, the time constant of $fsrGO_2$ is ~5 times smaller than that of $fsrGO_{500}$ (2.5 s). The high-frequency region (the inset plot in Figure 4b) is characterized by a small charge resistance and steep Nyquist curves, indicating that the surface of fsrGO is readily accessible. The equivalent series resistance (ESR) of $fsrGO_2$ and $fsrGO_{500}$ obtained from the intercept of the plot on the real axis is ~0.2 Ω and ~670 Ω cm^2, respectively. The enhanced performance (low τ and ESR) of ultraminiaturized fsrGO MSCs arises from the short diffusion pathways between adjacent elements of the interlaced electrodes and accessible diffusion channel formed by abundant mesopores. It is believed that the reduction extent of fsrGO can be further improved and time constant can be further reduced by choosing optimized laser parameters and utilizing some other hybrid techniques,[18] which needs intensive investigation in the future to make this innovative hybrid technique more robust. We also find that fs laser rGO MSCs show excellent cycling stability, retaining ~100% of their initial performance after 1000 charge/discharge cycles (see Figure 4c).

Figure 4d shows a Ragone plot comparing the performance of fs laser rGO MSCs with that of different energy storage devices used in high power microelectronics. fsrGO MSCs are characterized by extremely high volumetric specific capacitances (~105 F cm^{-3}) as well as high power densities (>10 W cm^{-3}) that are 3 orders of magnitude higher than in commercial Li-ion batteries[52] because MSCs contain a film of fsrGO with a thickness of only ~0.6 μm. In addition, these new MSCs demonstrate comparable power density to those obtained in an aluminum electrolytic capacitor,[16] while providing energy densities 10^3 times higher than those devices. The energy density is also a factor of 10 higher than that seen in graphene−carbon nanotube hybrid film MSCs[53] and 25 times higher than that in stackable graphene laser-induced MSC.[54] It is also 50 times higher than that found in 3D graphene supercapacitors (at comparable power density) formed by 3D printing.[55] These results show that mesoporous graphene electrodes, together with the miniaturization of microelectrode volume and

DOI: 10.1021/acsami.7b14410
ACS Appl. Mater. Interfaces 2018, 10, 5404−5412

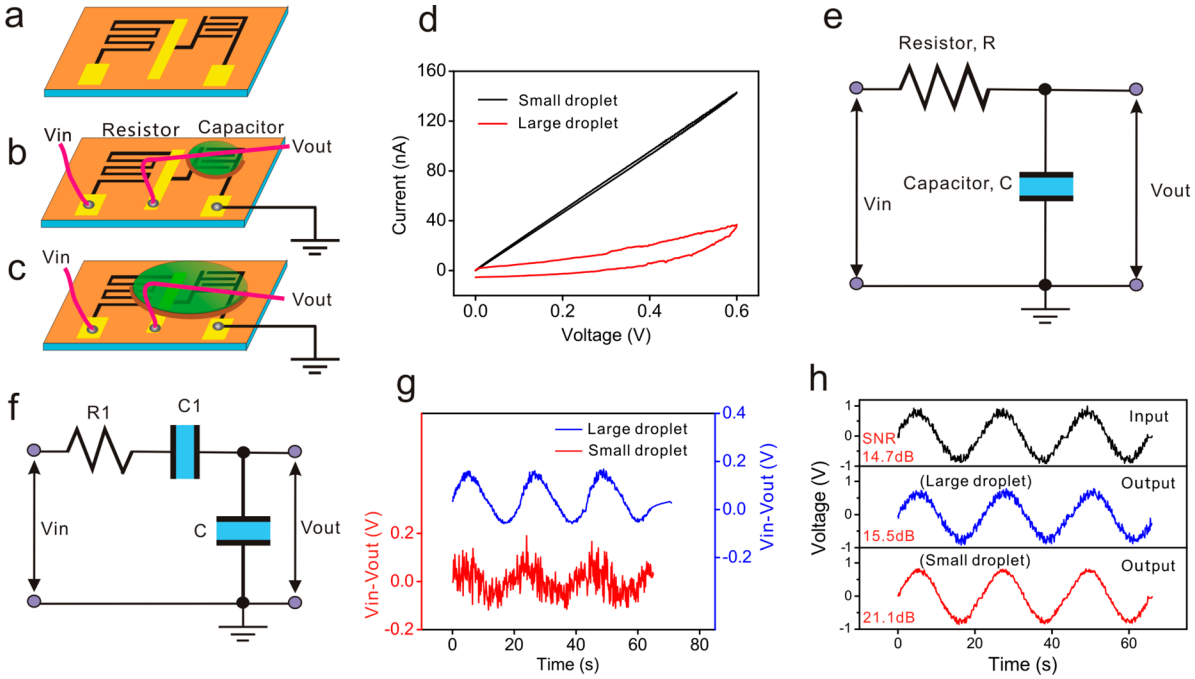

Figure 5. Practical applications in RC filter circuits of fsrGO MSCs with microelectrolyte gel transferred using fsLIFT. Schematic view of (a) connection of fsrGO resistor and MSC electrode, (b) all-graphene RC filter with precise coverage of small electrolyte droplet on fsrGO electrode, and (c) all-graphene RC filter with a large electrolyte droplet on fsrGO electrode. (d) *IV* curves for fs rGO resistor in (b) and (c). (e) and (f) Equivalent circuit diagrams for RC filter in (b) and (c), respectively. (g) Voltage signals across fsrGO resistor in (b) and (c) when applying a sinusoidal signal of 0.8 sin 0.174*t* with superimposed white noise. (h) Input signal and output signals across the fsrGO MSC in (b) and (c).

interelectrode space, optimizes the ionic diffusion dynamics, leading to higher power density. It is apparent that the high-performance ultraminiature MSCs fabricated by this new hybrid technique combining fs laser direct writing and accurate microdrops transfer may have many applications as energy storage units for powering compact micro/nano devices, which further enables the reduction of overall size of electronic systems.

To illustrate the priority of this ultraminiaturized MSC fabricated by this hybrid technique for practical encapsulation with other microelectronic components in ultrasmall microsystem applications, we have constructed an all-graphene RC filter written by a fs laser on a GO film. A simple first-order passive low pass filter can be made by connecting a single resistor together with a capacitor in series across an input signal (V_{in}), with the output of the filter (V_{out}), taken from the junction of capacitor. When a fs laser is introduced, the deoxygenation of GO during photochemical processing produces a dramatic increase in the conductivity of fs rGO which can be easily tuned by adjusting the laser fluence (Table S1). Thus, in an all-graphene RC filter circuit, directly written serpentine fsrGO can function as a resistor (Figure 5a–c and Figure S18). As for the capacitor involved in all graphene RC filter, two types of MSC have been constructed to compare the filter efficiency: (1) the as-prepared MSC with precise coverage of an electrolyte microdrop on fsrGO interlaced electrodes using fsLIFT (see Figure 5b); (2) a MSC having the same electrodes but covered by a large electrolyte drop that partially contacts fsrGO resistor nearby (see Figure 5c). As black curve shown in Figure 5d, the current–voltage (*IV*) curve of the as-written serpentine rGO resistor in Figure 5d exhibits a typical feature of perfect linear loop, indicating an ideal resistor having a resistance of ~4.3 MΩ. However, the *IV* curve of rGO resistor partially covered by large electrolyte drop (as shown in Figure 5c) exhibits a nearly rectangular loop (see the red curve in Figure 5d), which means resistor/electrolyte interference introduces capacitive impedance to fsrGO resistor. The above *IV* curves clearly suggest that the equivalent circuit diagrams for these two devices illustrated in Figures 5b and 5c should be the schemas as indicated in Figures 5e and 5f, respectively.

The input signal is set to be sum of a sinusoidal signal at 0.045 Hz and white noise (with amplitude of 0.1 V). According to the RC filter analysis (see Supporting Information), the intensity of the low-frequency sinusoidal signal remains almost constant while the high-frequency noise in the output signal, taken from the junction of the capacitor, should be greatly reduced. Therefore, the signal obtained from the voltage drop across the resistor (i.e., $V_{in} - V_{out}$) should consist of strong high-frequency noise. As estimated, the red curve in Figure 5g shows that the signal from the junction of the resistor without contamination by small electrolyte droplet (see Figure 5b) consists of a strong high-frequency noise component added to a very small sinusoidal signal. However, the signal from the resistor that has been partially covered by the large electrolyte droplet (as shown in Figure 5c) is a very weak high-frequency component added to a strong sinusoid signal (blue curve in Figure 5g). This different response indicates that the resistor/electrolyte interface greatly affects the efficiency with which white noise is filtered. Thus, the low pass filter without contact of electrolyte with resistor can increase the signal-to-noise ratio (SNR) from 14.7 to 21.1 dB (as shown in Figure 5h). However, the filter where the resistor has an interface with the large electrolyte droplet shows only a marginal increase in SNR to 15.5 dB.

The different electrical response of these two filters obviously arises from variations in the interface between the electrolyte droplet and the rGO resistor pattern. The part of the large electrolyte droplet that covers the rGO component within the

DOI: 10.1021/acsami.7b14410
ACS Appl. Mater. Interfaces 2018, 10, 5404–5412

serpentine rGO pattern introduces capacitive impedance into the rGO resistor. This term has a strong deleterious effect on the high-frequency filter capability for white noise. Hence, the output signal from this MSC still has a strong noise component. The characteristics of this signal are analyzed in detail in the Supporting Information. The above comparison clearly shows that the controllable microdroplet transfer technique shows obvious priority in microdevice design. Even though the performance of fsrGO MSCs can be further improved, the hybrid technique offers a versatile method to meet the gap between the miniaturization of microsystems and microdevice design.

CONCLUSIONS

We have developed a scalable direct-writing technology for the production of ultraminiature, fully solid-state, in-plane micro-supercapacitors (MSCs) using a hybrid technique that combines the reduction of graphene oxide with fs laser radiation (fsrGO) followed by precise transfer of electrolyte microdroplets via fsLIFT. The resulting mesoporous structure in graphene, together with a significant reduction in the width and separation distance of interlaced pads in electrodes, improves ionic diffusion and enhances electrochemical performance characteristics. These devices exhibit high specific capacitance, high energy and power densities, and high stability under cycling. The picoliter electrolyte microdroplets transferred under fsLIFT can be tailored to exactly cover individual MSC electrodes, avoiding interference that can occur when the electrolyte droplet overlaps with other electronic components in an ultracompact microdevice. An all-graphene resistor−capacitor (RC) filter is also constructed by combining the MSC and a fsrGO resistor, which is confirmed to exhibit highly enhanced performance characteristics. With their ultrasmall size and controllable fabrication process, the integrated fsrGO-MSCs devices engineered with this novel hybrid technique provides a versatile approach to meet the gap between the miniaturization of microsystems and microdevice design.

EXPERIMENTAL SECTION

Sample Preparation. Hummer's method[56] was used to synthesize GO from graphite powder (Nanjing XFNANO Materials Tech Co., Ltd.). An aqueous dispersion GO with a concertration of 0.5 mg mL^{-1} was prepared by sonification at low power for 10 min before being drop-cast on a silicon oxide substrate and annealed in air at 80 °C for 30 min. This resulted in a continuous GO film with a thickness of ∼500 nm. The GO-coated substrate was placed on an XYZ microscopy stage (Figure S1 in Supporting Information). We used a commercial fs laser system (Coherent Systems) delivering laser pulses at a central wavelength of 800 nm, with a maximum pulse energy of 4 mJ, and a pulse duration of 50 fs at repetition rate of 1 kHz. The fs laser pulses with an energy of 0.01 μJ were tightly focused using a microscope objective (Olympus) with ×100 magnification and a numerical aperture (NA) of 0.4 on the GO film to machine an array of rGO electrodes. A glass coated with 100 μm thick PVA-H_2SO_4 gel was placed at a distance of 500 μm above as-prepared rGO elecrtodes. The fs laser pulses with an energy of 4 μJ were focused through the glass using an objective (Olymbus) with ×10 magnification and a NA of 0.3 onto the electrolyte gel to generate single electrolyte microdrops. The location of droplets transferred on the rGO electrodes was verified from CCD camera images. The laser fluence was attenuated with a $\lambda/2$ plate together with a polarizer. Further details are given in the Supporting Information.

Materials Characterization. The microstructures and properties of GO and rGO in the device were investigated by means of field emission scanning electron microscopy (Zeiss EVO MA10), transmission electron microscopy (JEOL JEM 2010F), optical microscopy (Olymbus BX51), X-ray photoelectron spectroscopy (PHI Quantera II, with X-ray spot size of 7.5 μm), Raman spectra (LabRAMHR Evolution), and atom force microscopy (Veeco, dimension V).

Electrochemical Characterization. Electrochemical testing was undertaken on a CHI 660E electrochemical workstation connected through a probe station with tungsten probes (tip diameter = 10 μm) as the current collectors. CV tests were performed between 0 and 0.5 V at a scan rate of 1−1000 mV s^{-1} and EIS recorded in the frequency between 0.1 Hz and 10 kHz with an amplitude of 5 mV. Galvanostatic charge/discharge measurements were carried out in a range between 0 and 1 V at current densities of 5, 20, and 50 mA cm^{-2}. The whole testing processes were checked by the CCD camera of the microscope. The tests were conducted over three times carefully to make sure that the data were not obtained occasionally. The PVA−H_2SO_4 gel electrolyte was prepared by mixing 6 g of PVA and 6 g of H_2SO_4 in 60 mL of deionized water followed by heating up to 80 °C for 1 h together with vigorous stirring.[28] Calculations of the electrochemical performance are described in detail in the Supporting Information.

ASSOCIATED CONTENT

Supporting Information

The Supporting Information is available free of charge on the ACS Publications website at DOI: 10.1021/acsami.7b14410.

Femtosecond laser setup; details of micro-supercapacitors fabrication, graphene resistor−capacitor filter fabrication, electrochemical performance calculations and low pass resistor−capacitor analysis; AFM images of GO and fsrGO; SEM and TEM images of GO; electrolyte microdrop diameter vs laser fluence; conductivity of fsrGO vs laser fluence; description of edge effect (PDF)

AUTHOR INFORMATION

Corresponding Author

*E-mail: liulei@tsinghua.edu.cn (L.L.).

ORCID

Daozhi Shen: 0000-0002-5426-4357

Lei Liu: 0000-0002-3368-5136

Notes

The authors declare no competing financial interest.

ACKNOWLEDGMENTS

This work was supported by National Natural Science Foundation of China (51520105007, 51775299) and National Key Research and Development Program of China (2017YFB1104900). We thank Prof. Hongwei Zhu for assistance of electrical property measurements and thank Mr. Ming Xiao for helpful discussions.

REFERENCES

(1) Rocchitta, G.; Secchi, O.; Alvau, M. D.; Migheli, R.; Calia, G.; Bazzu, G.; Farina, D.; Desole, M. S.; O'Neill, R. D.; Serra, P. A. Development and Characterization of an Implantable Biosensor for Telemetric Monitoring of Ethanol in the Brain of Freely Moving Rats. *Anal. Chem.* **2012**, *84*, 7072−7079.

(2) Heo, Y. J.; Takeuchi, S. Towards Smart Tattoos: Implantable Biosensors for Continuous Glucose Monitoring. *Adv. Healthcare Mater.* **2013**, *2*, 43−56.

(3) Sykes, E. A.; Albanese, A.; Chan, W. C. W. Biophotonics: Implantable Waveguides. *Nat. Photonics* **2013**, *7*, 940−941.

(4) Koh, A.; Lu, Y.; Schoenfisch, M. H. Fabrication of Nitric Oxide-Releasing Porous Polyurethane Membranes-Coated Needle-Type Implantable Glucose Biosensors. *Anal. Chem.* **2013**, *85*, 10488−10494.

DOI: 10.1021/acsami.7b14410
ACS Appl. Mater. Interfaces 2018, 10, 5404−5412

(5) Sitti, M. Miniature devices: Voyage of the Microrobots. *Nature* **2009**, *458*, 1121−1122.
(6) Jager, E. W.; Inganäs, O.; Lundström, I. Microrobots for Micrometer-Size Objects in Aqueous Media: Potential Tools for Single-Cell Manipulation. *Science* **2000**, *288*, 2335−2338.
(7) Nelson, B. J.; Kaliakatsos, I. K.; Abbott, J. J. Microrobots for Minimally Invasive Medicine. *Annu. Rev. Biomed. Eng.* **2010**, *12*, 55−85.
(8) Solgaard, O.; Godil, A. A.; Howe, R. T.; Lee, L. P.; Peter, Y. A.; Zappe, H. Optical MEMS: From Micromirrors to Complex Systems. *J. Microelectromech. Syst.* **2014**, *23*, 517−538.
(9) Lessing, J.; Glavan, A. C.; Walker, S. B.; Keplinger, C.; Lewis, J. A.; Whitesides, G. M. Inkjet Printing of Conductive Inks with High Lateral Resolution on Omniphobic "RF Paper" for Paper-Based Electronics and MEMS. *Adv. Mater.* **2014**, *26*, 4677−4682.
(10) Martin-Olmos, C.; Rasool, H. I.; Weiller, B. H.; Gimzewski, J. K. Graphene MEMS: AFM Probe Performance Improvement. *ACS Nano* **2013**, *7*, 4164−4170.
(11) Kuang, S. Y.; Chen, J.; Cheng, X. B.; Zhu, G.; Wang, Z. L. Two-Dimensional Rotary Triboelectric Nanogenerator as a Portable and Wearable Power Source for Electronics. *Nano Energy* **2015**, *17*, 10−16.
(12) Kadivar, Z.; Beck, C. E.; Rovekamp, R. N.; O'Malley, M. K.; Joyce, C. A. On the Efficacy of Isolating Shoulder and Elbow Movements with a Soft, Portable, and Wearable Robotic Device. In *Wearable Robotics: Challenges and Trends*; Springer International Publishing: 2017; pp 89−93.
(13) Huang, P.; Lethien, C.; Pinaud, S.; Brousse, K.; Laloo, R.; Turq, V.; Respaud, M.; Demortière, A.; Daffos, B.; Taberna, P.; et al. On-Chip and Freestanding Elastic Carbon Films for Micro-Supercapacitors. *Science* **2016**, *351*, 691−695.
(14) Cao, L.; Yang, S.; Gao, W.; Liu, Z.; Gong, Y.; Ma, L.; Shi, G.; Lei, S.; Zhang, Y.; Zhang, S.; Vajtai, R.; Ajayan, P. M. Direct Laser-Patterned Micro-Supercapacitors from Paintable MoS_2 Films. *Small* **2013**, *9*, 2905−2910.
(15) Wu, Z. S.; Feng, X.; Cheng, H. M. Recent Advances in Graphene-Based Planar Micro-Supercapacitors for On-Chip Energy Storage. *Natl. Sci. Rev.* **2014**, *1*, 277−292.
(16) El-Kady, M. F.; Kaner, R. B. Scalable Fabrication of High-Power Graphene Micro-Supercapacitors for Flexible and On-Chip Energy Storage. *Nat. Commun.* **2013**, *4*, 1475.
(17) Wu, Z. S.; Parvez, K.; Feng, X.; Mullen, K. Graphene-Based In-Plane Micro-Supercapacitors with High Power and Energy Densities. *Nat. Commun.* **2013**, *4*, 2487.
(18) Li, R. Z.; Peng, R.; Kihm, K. D.; Bai, S.; Bridges, D.; Tumuluri, U.; Wu, Z.; Zhang, T.; Compagnini, G.; Feng, Z.; Hu, A. High-Rate In-Plane Micro-Supercapacitors Scribed onto Photo Paper Using *in situ* Femtolaser-Reduced Graphene Oxide/Au Nanoparticle Microelectrodes. *Energy Environ. Sci.* **2016**, *9*, 1458−1467.
(19) Chang, J.; Adhikari, S.; Lee, T. H.; Li, B.; Yao, F.; Pham, D. T.; Le, V. T.; Lee, Y. H. Leaf Vein-Inspired Nanochanneled Graphene Film for Highly Efficient Micro-Supercapacitors. *Adv. Energy Mater.* **2015**, *5*, 1500003.
(20) Liu, W.; Lu, C.; Wang, X.; Tay, R. Y.; Tay, B. K. High-Performance Micro-Supercapacitors Based on Two-Dimensional Graphene/Manganese Dioxide/Silver Nanowire Ternary Hybrid Film. *ACS Nano* **2015**, *9*, 1528−1542.
(21) Sun, L.; Wang, X.; Zhang, K.; Zou, J.; Zhang, Q. Metal-free SWNT/Carbon/MnO_2 Hybrid Electrode for High Performance Coplanar Micro-Supercapacitors. *Nano Energy* **2016**, *22*, 11−18.
(22) Wang, X.; Myers, B. D.; Yan, J.; Shekhawat, G.; Dravid, V.; Lee, P. S. Manganese Oxide Micro-Supercapacitors with Ultra-High Areal Capacitance. *Nanoscale* **2013**, *5*, 4119−4122.
(23) Ferris, A.; Garbarino, S.; Guay, D.; Pech, D. 3D RuO_2 Microsupercapacitors with Remarkable Areal Energy. *Adv. Mater.* **2015**, *27*, 6625−6629.
(24) Hwang, J. Y.; El-Kady, M. F.; Wang, Y.; Wang, L.; Shao, Y.; Marsh, K.; Ko, J. M.; Kaner, R. B. Direct Preparation and Processing of Graphene/RuO_2 Nanocomposite Electrodes for High-Performance Capacitive Energy Storage. *Nano Energy* **2015**, *18*, 57−70.
(25) Lu, X.; Liu, T.; Zhai, T.; Wang, G.; Yu, M.; Xie, S.; Ling, Y.; Liang, C.; Tong, Y.; Li, Y. Improving the Cycling Stability of Metal-Nitride Supercapacitor Electrodes with a Thin Carbon Shell. *Adv. Energy Mater.* **2014**, *4*, 1300994.
(26) Wang, X.; Yan, C.; Sumboja, A.; Yan, J.; Lee, P. S. Achieving High Rate Performance in Layered Hydroxide Supercapacitor Electrodes. *Adv. Energy Mater.* **2014**, *4*, 1301240.
(27) Meng, C.; Maeng, J.; John, S. W. M.; Irazoqui, P. P. Ultrasmall Integrated 3D Micro-Supercapacitors Solve Energy Storage for Miniature Devices. *Adv. Energy Mater.* **2014**, *4*, 1301269.
(28) Lobo, D. E.; Banerjee, P. C.; Easton, C. D.; Majumder, M. Miniaturized Supercapacitors: Focused Ion Beam Reduced Graphene Oxide Supercapacitors with Enhanced Performance Metrics. *Adv. Energy Mater.* **2015**, *5*, 1500665.
(29) Florian, C.; Caballero-Lucas, F.; Fernández-Pradas, J.; Artigas, R.; Ogier, S.; Karnakis, D.; Serra, P. Conductive Silver Ink Printing Through the Laser-Induced Forward Transfer Technique. *Appl. Surf. Sci.* **2015**, *336*, 304−308.
(30) Shen, D.; Zou, G.; Liu, L.; Duley, W. W.; Zhou, Y. N. Investigation of Splashing Phenomena During the Impact of Molten Sub-Micron Gold Droplets on Solid Surfaces. *Soft Matter* **2016**, *12*, 295−301.
(31) Zywietz, U.; Evlyukhin, A. B.; Reinhardt, C.; Chichkov, B. N. Laser Printing of Silicon Nanoparticles with Resonant Optical Electric and Magnetic Responses. *Nat. Commun.* **2014**, *5*, 3402.
(32) Fernández-Pradas, J.; Florian, C.; Caballero-Lucas, F.; Sopeña, P.; Morenza, J.; Serra, P. Laser-Induced Forward Transfer: Propelling Liquids with Light. *Appl. Surf. Sci.* **2017**, *418*, 559−564.
(33) Delaporte, P.; Alloncle, A. P. [INVITED] Laser-Induced Forward Transfer: A High Resolution Additive Manufacturing Technology. *Opt. Laser Technol.* **2016**, *78*, 33−41.
(34) Vespini, V.; Coppola, S.; Todino, M.; Paturzo, M.; Bianco, V.; Grilli, S.; Ferraro, P. Forward Electrohydrodynamic Inkjet Printing of Optical Microlenses on Microfluidic Devices. *Lab Chip* **2016**, *16*, 326−333.
(35) Zhang, Y.; Guo, L.; Wei, S.; He, Y.; Xia, H.; Chen, Q.; Sun, H. B.; Xiao, F. S. Direct Imprinting of Microcircuits on Graphene Oxides Film by Femtosecond Laser Reduction. *Nano Today* **2010**, *5*, 15−20.
(36) Sokolov, D. A.; Shepperd, K. R.; Orlando, T. M. Formation of Graphene Features from Direct Laser-Induced Reduction of Graphite Oxide. *J. Phys. Chem. Lett.* **2010**, *1*, 2633−2636.
(37) Lobo, D. E.; Fu, J.; Gengenbach, T.; Majumder, M. Localized Deoxygenation and Direct Patterning of Graphene Oxide Films by Focused Ion Beams. *Langmuir* **2012**, *28*, 14815−14821.
(38) Ferrari, A. C.; Robertson, J. Interpretation of Raman Spectra of Disordered and Amorphous Carbon. *Phys. Rev. B: Condens. Matter Mater. Phys.* **2000**, *61*, 14095.
(39) Ferrari, A.; Robertson, J. Resonant Raman Spectroscopy of Disordered, Amorphous, and Diamondlike Carbon. *Phys. Rev. B: Condens. Matter Mater. Phys.* **2001**, *64*, 075414.
(40) Xu, Y.; Chen, C. Y.; Zhao, Z.; Lin, Z.; Lee, C.; Xu, X.; Wang, C.; Huang, Y.; Shakir, M. I.; Duan, X. Solution Processable Holey Graphene Oxide and Its Derived Macrostructures for High-Performance Supercapacitors. *Nano Lett.* **2015**, *15*, 4605−4610.
(41) Kim, H. K.; Bak, S. M.; Lee, S. W.; Kim, M. S.; Park, B.; Lee, S. C.; Choi, Y. J.; Jun, S. C.; Han, J. T.; Nam, K. W.; Chung, K. Y.; Wang, J.; Zhou, J.; Yang, X. Q.; Roh, K. C.; Kim, K. B. Scalable Fabrication of Micron-Scale Graphene Nanomeshes for High-Performance Supercapacitor Applications. *Energy Environ. Sci.* **2016**, *9*, 1270−1281.
(42) Russo, P.; Hu, A.; Compagnini, G.; Duley, W. W.; Zhou, N. Y. Femtosecond Laser Ablation of Highly Oriented Pyrolytic Graphite: a Green Route for Large-Scale Production of Porous Graphene and Graphene Quantum Dots. *Nanoscale* **2014**, *6*, 2381−2389.
(43) Cheng, H.; Liu, J.; Zhao, Y.; Hu, C.; Zhang, Z.; Chen, N.; Jiang, L.; Qu, L. Graphene Fibers with Predetermined Deformation as Moisture-Triggered Actuators and Robots. *Angew. Chem., Int. Ed.* **2013**, *52*, 10482−10486.

DOI: 10.1021/acsami.7b14410
ACS Appl. Mater. Interfaces 2018, 10, 5404−5412

(44) Borini, S.; White, R.; Wei, D.; Astley, M.; Haque, S.; Spigone, E.; Harris, N.; Kivioja, J.; Ryhanen, T. Ultrafast Graphene Oxide Humidity Sensors. *ACS Nano* **2013**, *7*, 11166−11173.
(45) Dikin, D. A.; Stankovich, S.; Zimney, E. J.; Piner, R. D.; Dommett, G. H.; Evmenenko, G.; Nguyen, S. T.; Ruoff, R. S. Preparation and Characterization of Graphene Oxide Paper. *Nature* **2007**, *448*, 457−460.
(46) Chin, S.; Lagacé, S. Generation of H_2, O_2, and H_2O_2 from Water by the Use of Intense Femtosecond Laser Pulses and the Possibility of Laser Sterilization. *Appl. Opt.* **1996**, *35*, 907−911.
(47) Zhu, J.; Childress, A. S.; Karakaya, M.; Dandeliya, S.; Srivastava, A.; Lin, Y.; Rao, A. M.; Podila, R. Defect-Engineered Graphene for High-Energy- and High-Power-Density Supercapacitor Devices. *Adv. Mater.* **2016**, *28*, 7185−7192.
(48) Marken, F.; Neudeck, A.; Bond, A.; Scholz, F. In *Electroanalytical Methods: Guide to Experiments and Applications*; Scholz, F., Ed.; Springer-Verlag: Berlin, 2010; pp 74−78.
(49) Banks, C. E.; Davies, T. J.; Wildgoose, G. G.; Compton, R. G. Electrocatalysis at Graphite and Carbon Nanotube Modified Electrodes: Edge-Plane Sites and Tube Ends Are the Reactive Sites. *Chem. Commun.* **2005**, *7*, 829−841.
(50) Ekiz, O. O.; Urel, M.; Guner, H.; Mizrak, A. K.; Dana, A. Reversible Electrical Reduction and Oxidation of Graphene Oxide. *ACS Nano* **2011**, *5*, 2475−2482.
(51) In, J. B.; Hsia, B.; Yoo, J. H.; Hyun, S.; Carraro, C.; Maboudian, R.; Grigoropoulos, C. P. Facile Fabrication of Flexible All Solid-State Micro-Supercapacitor by Direct Laser Writing of Porous Carbon in Polyimide. *Carbon* **2015**, *83*, 144−151.
(52) Pech, D.; Brunet, M.; Durou, H.; Huang, P.; Mochalin, V.; Gogotsi, Y.; Taberna, P. L.; Simon, P. Ultrahigh-Power Micrometre-Sized Supercapacitors Based on Onion-Like Carbon. *Nat. Nanotechnol.* **2010**, *5*, 651−654.
(53) Wen, F.; Hao, C.; Xiang, J.; Wang, L.; Hou, H.; Su, Z.; Hu, W.; Liu, Z. Enhanced Laser Scribed Flexible Graphene-Based Micro-Supercapacitor Performance with Reduction of Carbon Nanotubes Diameter. *Carbon* **2014**, *75*, 236−243.
(54) Peng, Z.; Lin, J.; Ye, R.; Samuel, E. L.; Tour, J. M. Flexible and Stackable Laser-Induced Graphene Supercapacitors. *ACS Appl. Mater. Interfaces* **2015**, *7*, 3414−3419.
(55) Zhu, C.; Liu, T.; Qian, F.; Han, T. Y.; Duoss, E. B.; Kuntz, J. D.; Spadaccini, C. M.; Worsley, M. A.; Li, Y. Supercapacitors Based on Three-Dimensional Hierarchical Graphene Aerogels with Periodic Macropores. *Nano Lett.* **2016**, *16*, 3448−3456.
(56) Hummers, W. S., Jr.; Offeman, R. E. Preparation of Graphitic Oxide. *J. Am. Chem. Soc.* **1958**, *80*, 1339−1339.

DOI: 10.1021/acsami.7b14410
ACS Appl. Mater. Interfaces 2018, 10, 5404−5412